Supplementary Information

Optimizing $MnNi_2S_4$ Electrode Performance via Sulfur Precursor Selection: A Comparative Study for High-Rate Supercapacitor Applications

Malashri Boraiah Sannaobaiah[a], Sharath Kumar Basavaraju[a], Gireesh kumar Basavaraj Chavati[a], Krishna Venkatesh[b], Muralidhara Handanahalli Basavarajaiah[b*], Arthoba Nayaka Yanjerappa[a*]

[a] Department of Chemistry, School of Chemical Science, Kuvempu University, Shankaraghatta 577451, Shivamogga, Karnataka, India

[b] Centre for Incubation, Innovation, Research and Consultancy (CIIRC), Jyothy Institute of Technology, Thataguni, Off Kanakapura Main Road, Bangalore 560082, India

[*]Corresponding authors

E-mail address: muralidhara.hb@ciirc.jyothyit.ac.in (Dr. Muralidhara H B)

E-mail address: drarthoba@gmail.com(Dr. Arthoba Nayaka Y)

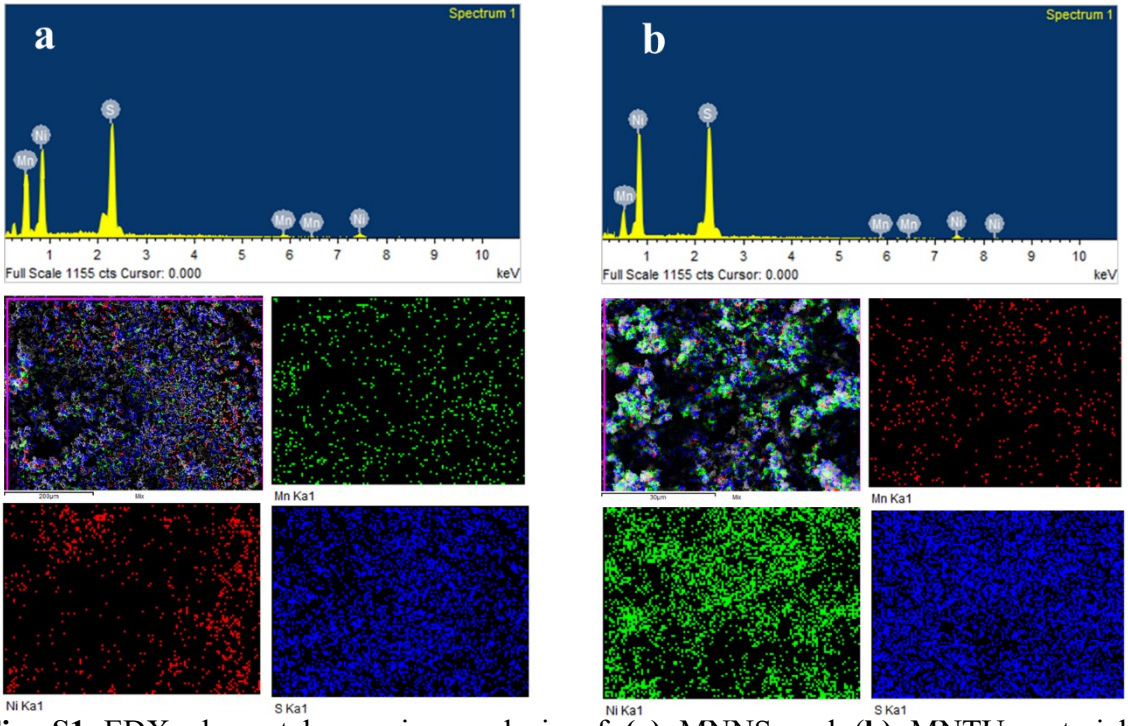

Fig. S1 EDX elemental mapping analysis of **(a)** MNNS and **(b)** MNTU materials, respectively.

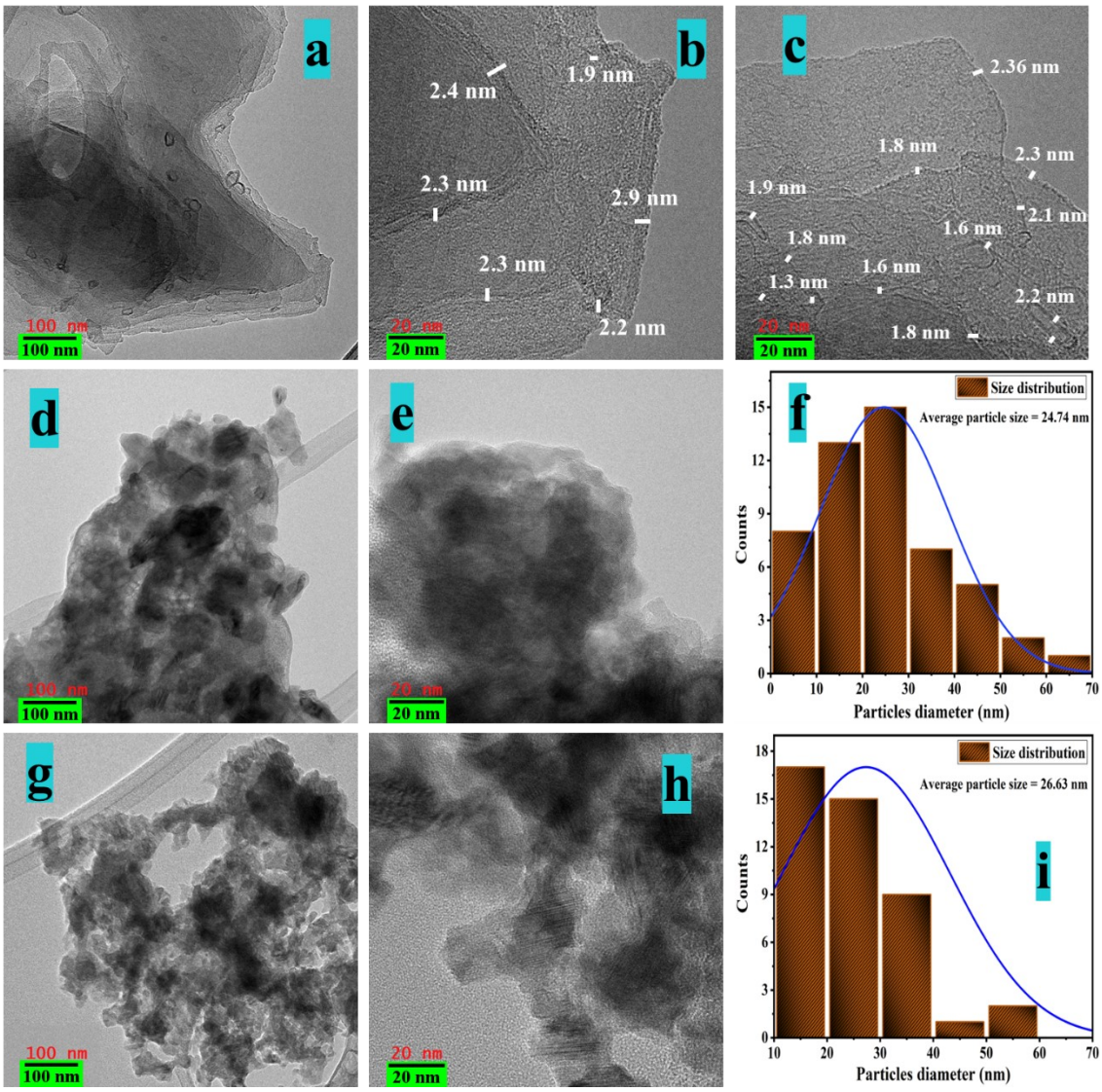

Fig. S2 TEM images of **(a-c)** MNTA, **(d-e)** MNNS, and **(g-h)** MNTU samples, respectively; **(f)** and **(i)** Average particle size distribution graphs of MNNS and MNTU samples, respectively.

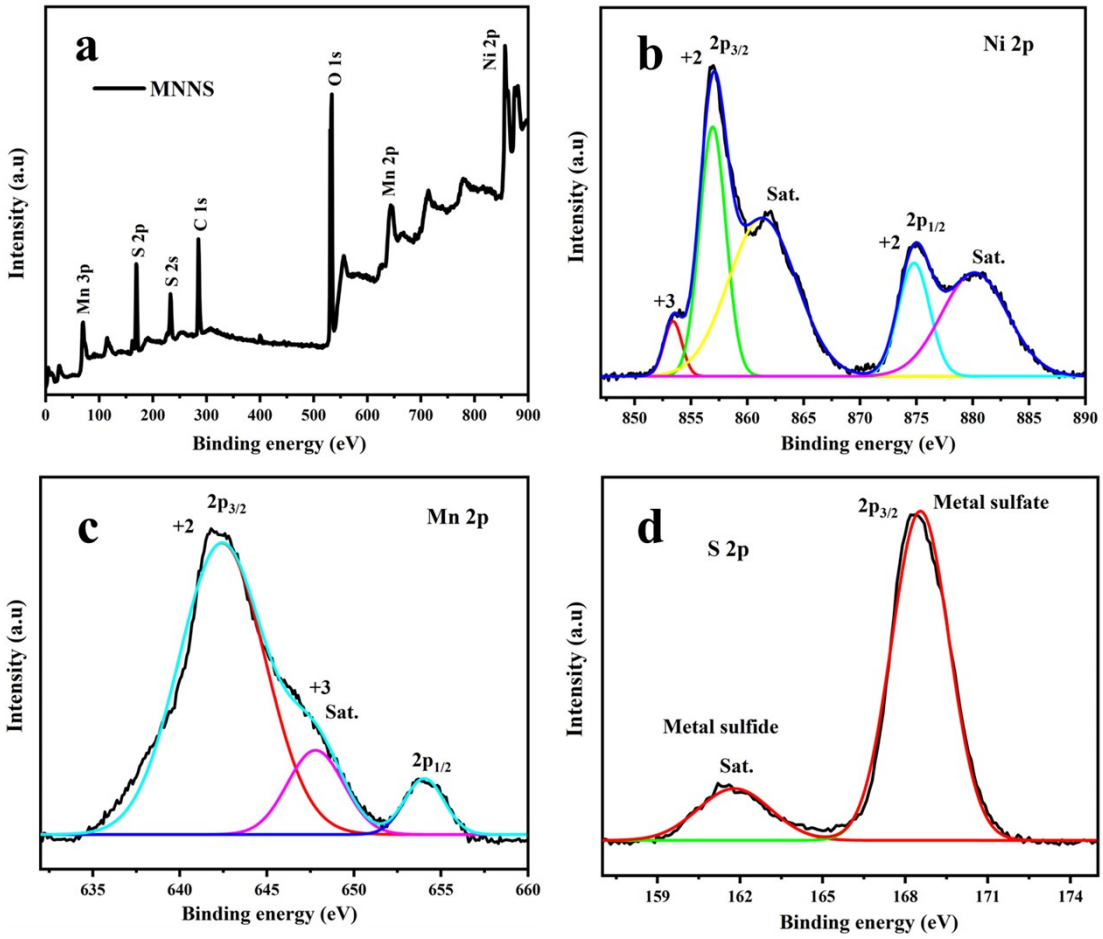

Fig. S3 (a) XPS survey spectra of MNNS, High-resolution XPS scans of **(b)** Ni 2p, **(c)** Mn 2p and **(d)** S 2p elements of MNNS sample respectively.

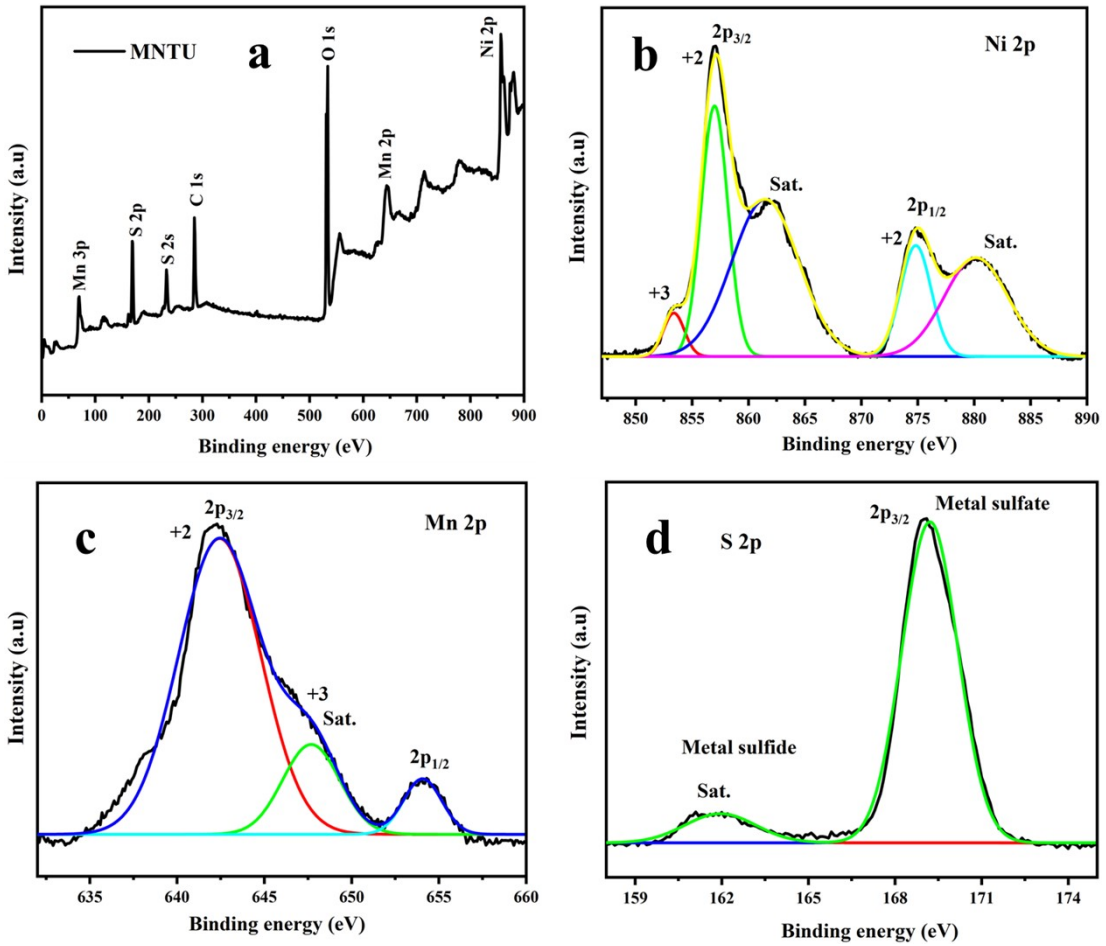

Fig. S4 (a) XPS survey spectra of MNTU, High-resolution XPS scans of **(b)** Ni 2p, **(c)** Mn 2p and **(d)** S 2p elements of MNTU sample respectively.

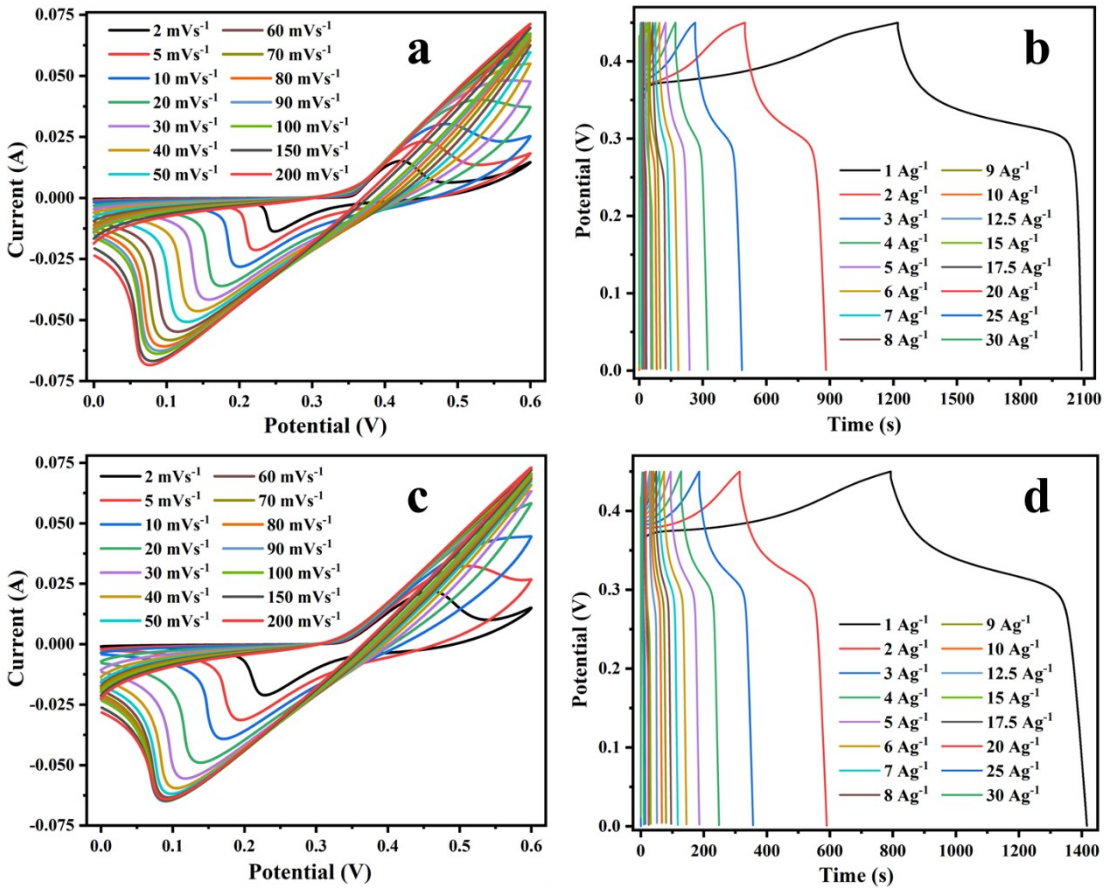

Fig. S5 (a) and **(b)** CV and GCD plots of MNNS, and (**c**) and **(d)** CV and GCD plots of MNTU at various scan rates and at various current densities, respectively.

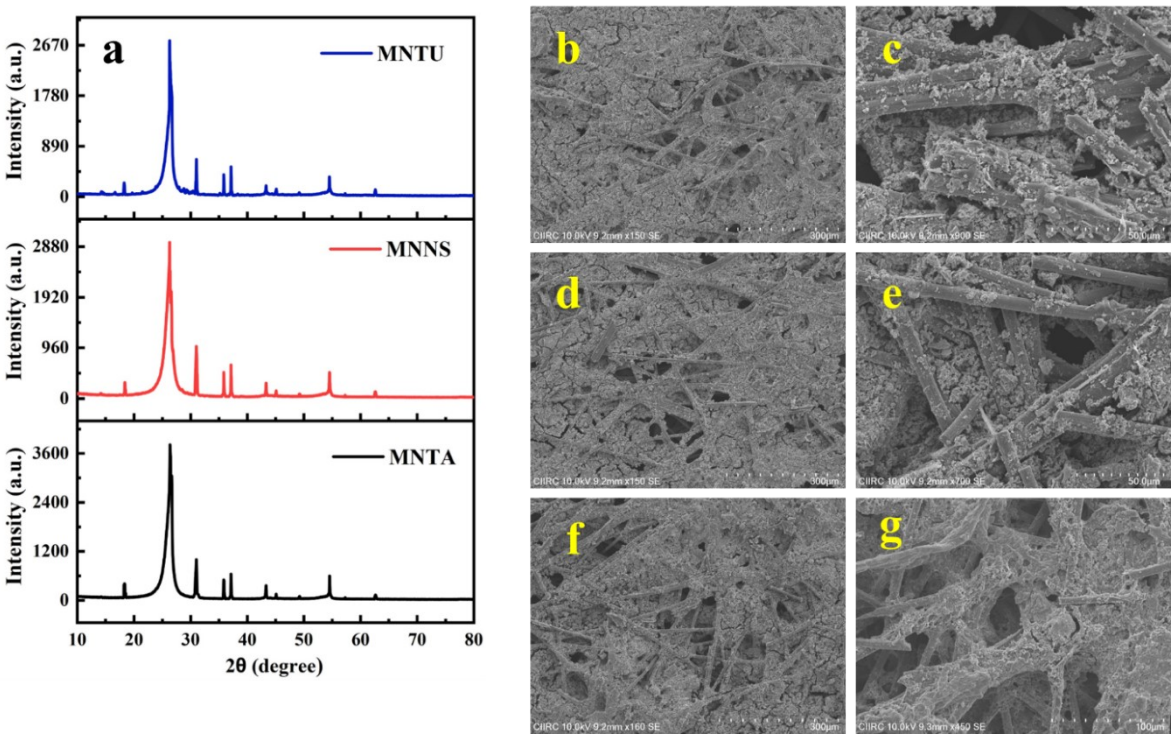

Fig. S6 (**a)** XRD graph of the MNTA, MNNS, and MNTU; SEM images of **(b-c)** MNTA; **(d-e)** MNNS; and **(f-g)** MNTU material deposited Toray carbon after cycle studies, respectively.

Table S1 The respective capacitance, energy, and power density performance comparison of the MNTA//MNTA//KOH Symmetric supercapacitor device with other similar electrode materials

Material	**Specific capacitance (F/g)**	**Energy density (Wh/kg)**	**Power density (W/kg)**	**Potential window (V)**	**Life cycles**	**References**
Ni-Mn-S//AC	129.4	40.4	750	0-1.5 V	10,000 85.5%	18
Ni-Mn-S-rGO//AC	64	22.76	400	0-1.6 V	5000 86.3%	19
CoMnNiS //NiCuO	20.8	8.4	985	0-1.7 V	-	22
Ni-Mn-S//rGO	108	36	775	0-1.55V	1500 90%	28
MnNiS@Mxene//AC	307.18	34.79	1142.61	0-1.6 V	7000 87.57%	42
MNTA//MNTA	**136.9**	**54.95**	**1274.92**	**0-1.7 V**	**5000**	**Present**

	90.55%	**work**

FTIR Analysis

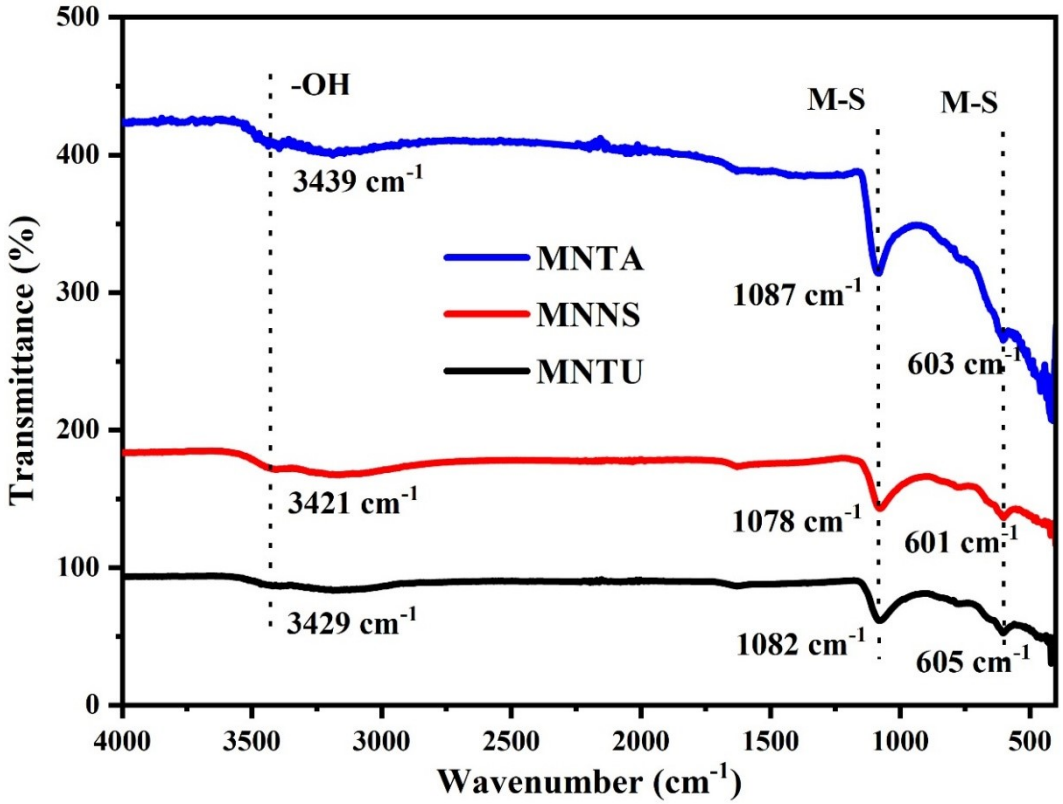

Fig. S7 FTIR spectra of the MNTA, MNNS, and MNTU samples.

The FTIR spectra of MNTA, MNNS, and MNTU samples (Fig. S7) were recorded to identify the surface functional groups and bonding characteristics. A slight shift in the FTIR peak positions was observed among the three samples, particularly in the 603, 601, 605 cm^{-1} and 1087, 1078, 1082 cm^{-1} region corresponding to symmetrical and asymmetrical stretching vibrations metal–sulfur (M–S, M= Mn and Ni), respectively, confirming the formation of the metal sulphide framework[25,31,35,50]. These small shifts can be attributed to variations in local bonding environments, differences in crystallinity, and the nature of sulfur coordination resulting from the use of different sulfur precursors. The weak bands around 3439, 3421, 3429 cm^{-1} correspond to the stretching vibrations of adsorbed water molecules and surface hydroxyl groups[31,35]. The MNTU sample displays relatively more intense features across the spectrum, possibly due to residual surface species and higher defect content. In contrast, the MNTA spectrum exhibits sharper and better-resolved peaks, indicating higher crystallinity and a more ordered structure, while MNNS shows broader bands, consistent with its more defective and porous network. These observations align well with XRD and XPS results, confirming successful synthesis and providing complementary evidence of the bonding environment and surface functional groups present in the materials.